



Insights into the role of C-S-C bond in C_3N_5 for photocatalytic NO deep oxidation: Experimental and DFT exploration

Junlei Zhang ^a, Zhi Li ^b, Bin Liu ^b, Mengshan Chen ^c, Yingtang Zhou ^{c,*}, Mingshan Zhu ^{b,*}

^a State Key Laboratory of Solidification Processing, School of Materials Science and Engineering, Northwestern Polytechnical University, Xi'an 710072, PR China

^b Guangdong Key Laboratory of Environmental Pollution and Health, School of Environment, Jinan University, Guangzhou 511443, PR China

^c National Engineering Research Center for Marine Aquaculture, Marine Science and Technology College, Zhejiang Ocean University, Zhoushan, Zhejiang 316004, PR China



ARTICLE INFO

Keywords:

S-doped C_3N_5
Photogenerated carrier dynamics
Structural defects
Air NO
Deep oxidation

ABSTRACT

Non-stoichiometric polymer carbon nitride of C_3N_5 is becoming an important visible-light-type catalyst due to the narrow bandgap, non-toxicity, and thermal stability. Here, we report a sulfur doping strategy for upgrading the photogenerated carriers' dynamics of C_3N_5 . Studies on the transient diffuse reflectance spectra prove that the lifetime of photogenerated carriers of sulfur-doped C_3N_5 ($\text{S}-\text{C}_3\text{N}_5$) increases 61.6 %. The widened visible-light responsive range and enhanced structural defects are also confirmed by UV-vis DRS and ESR characterizations. DFT calculations also verify the better NO adsorption and activation as well as give an insight into the mechanism of NO conversion from the molecule level. Such unique properties endow $\text{S}-\text{C}_3\text{N}_5$ with a 4.9- and 5.1-fold increase in photocatalytic NO removal efficiency and rate respectively compared to C_3N_5 . *In-situ* DRIFTS tests demonstrate the excellent NO deep-oxidation capability of $\text{S}-\text{C}_3\text{N}_5$. Ten-cycle NO removal experiments prove its reusability and durability.

1. Introduction

Realizing the development of high-efficiency photocatalysts for environmental pollution control and energy conversion is a hot topic and remains a big challenge for practical applications. Very recently, polymer C_3N_5 with a non stoichiometric ratio of C/N is drawing increasing attention in the field of environmental photocatalysis due to the unique properties of wider visible-light response, better adsorption and activation for small molecules, and more structural defects in comparison to the most popular PCN of g- C_3N_4 [1–6]. However, the inherent low electrical conductivity, insufficient active sites, and unoptimized electronic structure still hinder the electron charge transfer of pristine C_3N_5 , further limiting its improvement in photocatalytic performance [7,8].

Up to date, several approaches including morphology structure control (e.g., nanorods and nanosheets) [5,9], element/ion doping (e.g., B, P, K, and K/I) [10–13], and heterojunction construction with other semiconductors (e.g., $\text{AgCl}(\text{PO}_4^3-/CO_3^{2-})$, $\text{Bi}_2\text{Mo}(\text{W})\text{O}_6$, $\text{Bi}_4\text{O}_5\text{Br}(\text{I})_2$, P25, NiCr-LDH, and g- C_3N_4) [14–32] have been employed to upgrade the photocatalytic performance of pristine C_3N_5 . The morphology structure control approach mainly focuses on the physical structure change. For

the heterojunction construction means, its key is usually to employ well the merits of another semiconductor to promote the separation and transfer of photogenerated electrons/holes. Above two strategies always overlook the tune of inherent properties of C_3N_5 self. In relative terms, element doping, especially no-metal sulfur element introduction can better and directly optimize the electronic structure of the semiconductor self to achieve a wider light-response range, more efficient separation and transfer of photogenerated carriers, and better active sites, just as the same as verified by previous studies on g- C_3N_4 [33–37].

Moreover, only Hu et al. [12] and Li et al. [10], respectively investigated the effect of phosphorus or boron element doping on the photocatalytic performance of pristine C_3N_5 . Phosphorous atom is introduced into C_3N_5 by replacing with a carbon atom and exists in the form of $\text{P} - \text{N}/\text{P} = \text{N}$ bonds, where phosphorus 2p level as donor states can widen the range of visible-light response and upgrade the separation and transfer of photogenerated electrons/holes, finally achieving the better photocatalytic activity [12]. Boron atom found can occupy the carbon vacancies of pristine C_3N_5 , further optimizing band structure, upgrading the separation and transfer of photogenerated electrons/holes, and reinforcing the adsorption and activation towards N_2 , thus resulting in the improvement of the photocatalytic performance to

* Corresponding authors.

E-mail addresses: zhouyingtang@zjou.edu.cn (Y. Zhou), zhumingshan@jnu.edu.cn (M. Zhu).

synthesize NH₃ [10]. On one hand, although above reported studies don't investigate in-depth the improved photogenerated carrier dynamics of non-metal element doped C₃N₅, being lack more intrinsic cognition, they prove the feasibility of non-metal element doping for better C₃N₅. On other hand, to the best of our knowledge, studies on non-metal element doped C₃N₅ are rare, especially no studies on the exploration how sulfur doping affects the photo-activity of pristine C₃N₅.

In this work, we report the sulfur-doped C₃N₅ (S-C₃N₅) as a photocatalyst for the first time, which is synthesized by using dibenzyl disulfide and 3-amino-1,2,4-triazole as the resources. In the photocatalytic removal for air NO, S-C₃N₅ photocatalysts exhibit much higher performance than pristine C₃N₅, especially when S doping content is relatively low, the NO removal efficiency and rate respectively increase 4.9 folds and 5.1 folds to pristine C₃N₅. The transient diffuse reflectance spectra prove the significantly extended lifetime of photogenerated carriers of S-C₃N₅ than C₃N₅. The enhanced structural defects give more unpair electrons for NO/O₂ activation. Density function theory (DFT) calculations verify the better NO adsorption and activation, more electron transfer with NO, and visible-light response properties of S-C₃N₅. *In-situ* DRIFTS results demonstrate the excellent deep-oxidation capability for NO of S-C₃N₅. Ten cycle experiments clearly prove the stability and reusability of S-C₃N₅. A possible reaction mechanism of NO photo-oxidation over S-C₃N₅ is proposed. This work demonstrates the reasonability of sulfur doping for upgrading pristine C₃N₅ and in-depth explores the origin of S-C₃N₅ exhibiting better photo-activity.

2. Experimental details

2.1. Synthesis of sulfur-doped C₃N₅ (S-C₃N₅)

In detail, 3.2 g of 3-amino-1,2,4-triazole was first dissolved into 10 mL deionized water under thoroughly stirring. Then, a certain amount (for example, 0.1 mmol, 0.5 mmol, and 1 mmol) of dibenzyl disulfide

was added into above solution. After 4 h of stirring, the mixture was transferred to the drying oven and dried at 100 °C until the water was completely removed. The obtained sample was grounded into powder and then transferred into a muffle furnace for a temperature programmed treatment. The detailed conditions are the same as those employed in synthesizing bulk C₃N₅ [6]. The obtained sulfur-doped C₃N₅ samples are named as S-C₃N₅_0.1, S-C₃N₅_0.5, and S-C₃N₅_1, respectively.

In addition, the characterization methods of as-prepared catalysts, photoelectrochemical tests, performance evaluation, and density functional theory (DFT) calculations are available in the [Supporting information](#) file.

3. Results and discussion

3.1. Synthesis and characterization of C₃N₅ before and after sulfur doping

The sulfur-doped C₃N₅ (S-C₃N₅) catalysts were fabricated by using 3-amino-1,2,4-triazole and dibenzyl disulfide as the resources through a facile liquid-phase mixing-recrystallization-polymerization approach ([Scheme S1](#) and [Fig. 1A](#)). The morphology and nanostructure were initially investigated by the transmission electron microscope (TEM). As observed in [Fig. 1B-C](#), sulfur doping results in a dramatic change in the nanostructure, with a large number of tubular structures in S-C₃N₅_0.1. The BET surface area and average pore size ([Figure S1](#) and [1D](#)) calculated from the N₂adsorption-desorption isotherms respectively show a 13.2-fold increase and 2.2-fold decrease after sulfur doping, suggesting more reaction sites can be provided, which contributes to the NO catalytic conversion.

Whether the sulfur element is doped or not and the existing form of sulfur in S-C₃N₅ are studied by the survey and high-resolution X-ray photoelectron spectra (XPS). By comparing the survey XPS ([Fig. 2 A](#) and [S2A](#)), the peak belonging to S 2p is observed, demonstrating successful S

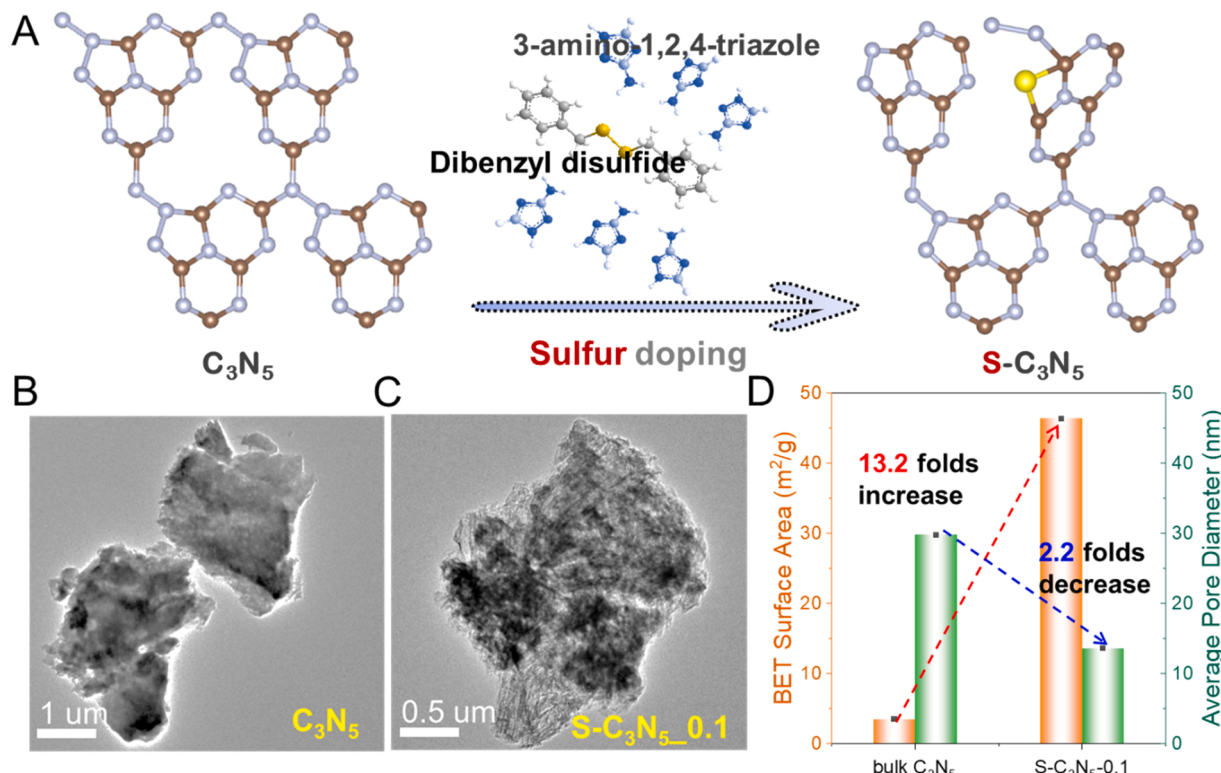


Fig. 1. (A) The schematic diagram for the synthesis of sulfur-doped C₃N₅, (B-C) transmission electron microscopy (TEM) images of C₃N₅ and S-C₃N₅_0.1, and (D) the comparison of their BET surface areas and average pore diameters.

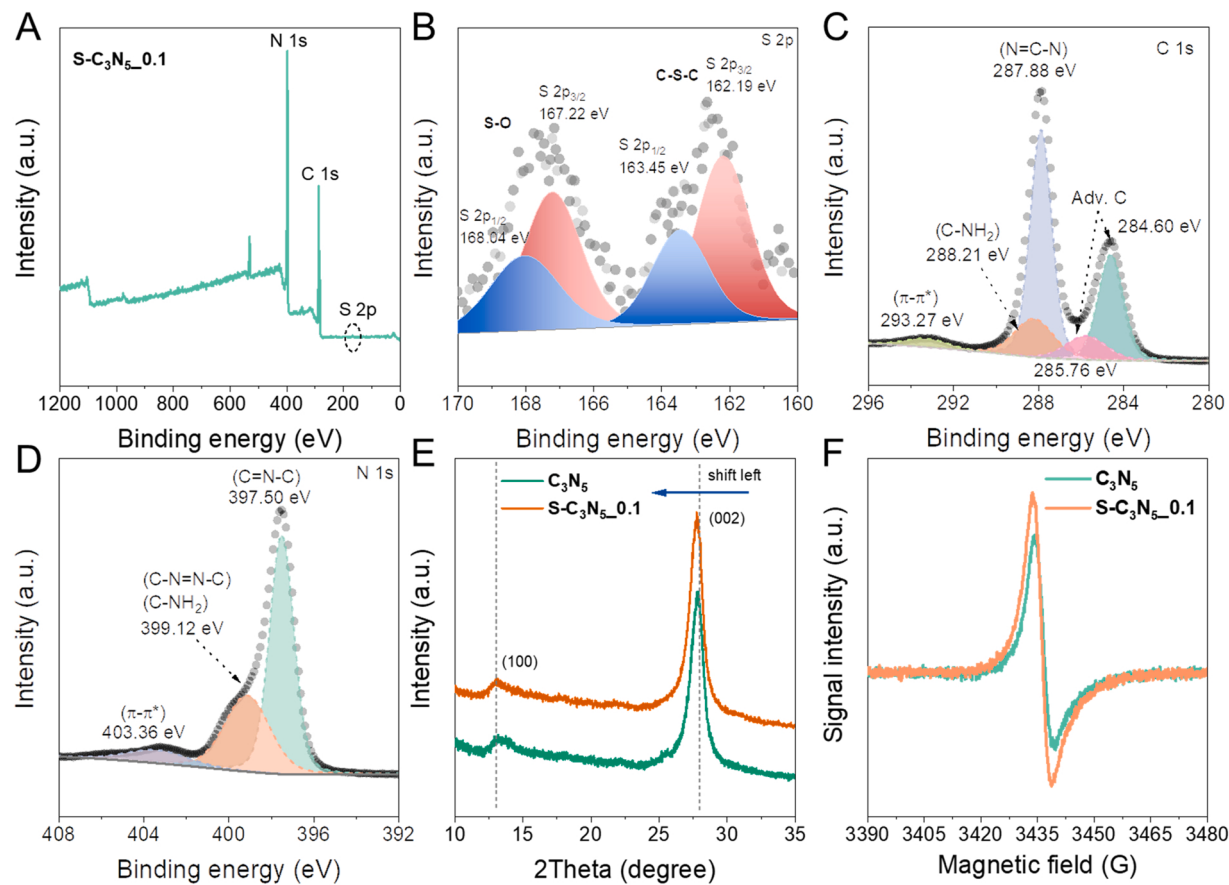


Fig. 2. (A) Survey X-ray photoelectron spectroscopy (XPS), (B) S 2p, (C) C 1 s, and (D) N 1 s high-resolution XPS of S-C₃N₅_0.1. (E) X-ray diffraction (XRD) patterns and (F) electron spin resonance (ESR) spectra of C₃N₅ and S-C₃N₅_0.1.

doping. From the high-resolution XPS of S 2p in Fig. 2 B, it can be seen that S exists in the form of C-S-C and S-O groups, especially the former proves that the S atom is indeed introduced into the C-N frame of the C₃N₅ via replacing with the N atom. Furthermore, by comparing the high-resolution XPS spectra of C 1 s and N 1 s (Fig. 2 C-D and S2B-C), we can see that S doping does not change the types of functional groups involving C and N (e.g., N=C-N, C-NH₂, C≡N-C, C-N=N-C), but makes their binding energies shift to a lower level, which indicates an internal electric field existing in S-C₃N₅. X-ray diffraction (XRD) patterns shown in Fig. 2E and S3 indicate that pristine C₃N₅ and S-C₃N₅ present two peaks belonging to crystal planes of (100) and (002), but the special thing is that the (002) peak of S-C₃N₅ shows a left shift to that of C₃N₅, suggesting its more loosely stacked interlayer distance, which consists with the results of TEM and BET surface area. Moreover, the electron spin resonance (ESR) spectra of C₃N₅ and S-C₃N₅_0.1 exhibit S doping increases the intensity of the unpaired electrons, implying the enriched structural defects in S-C₃N₅.

The transient diffuse reflectance spectra of C₃N₅ and S-C₃N₅_0.1 collected on the time-resolved diffuse reflectance spectroscopy were further employed to identify the influence of S doping in C₃N₅ for the behavior of photogenerated carriers. From Fig. 3A-B, it was found that S doping does not change the location of the adsorption peak, i.e., the adsorption peaks of C₃N₅ and S-C₃N₅_0.1 locate at 550 nm when using an excitation light with a 410 nm wavelength. Usually, the absorption of photogenerated holes takes place in the region from 540 nm to 620 nm [38,39]. Thus, here, the broad adsorption at 450–700 nm of C₃N₅ and S-C₃N₅_0.1 ascribes to the adsorption of the photogenerated holes. For a photocatalyst, it is important to investigate the dynamics of photogenerated carriers due to their key role in photo activity [40–42]. We further investigated the dynamics of photogenerated holes at a probe

wavelength of 550 nm (Fig. 3C-D). The kinetic traces fitted by the model of ExpDecay2 with a equation of $y = y_0 + A_1 * \exp(-(x-x_0)/t_1) + A_2 * \exp(-(x-x_0)/t_2)$ are summarized in Table S1. It can be found that S-C₃N₅_0.1 exhibits the slower decay of photogenerated holes, where the average lifetime (75.3 ps) of photogenerated holes is around 1.6 folds that of pristine C₃N₅, indicating that excited photogenerated carriers in S-C₃N₅ are more probable to diffuse and react with the surface adsorbed O₂ and even the target NO molecules.

Fig. 4 A shows the comparison of the photocurrent response of S-C₃N₅_0.1 and pristine C₃N₅. During the six runs, the photocurrent density of S-C₃N₅_0.1 respectively increases 9.9, 5.7, 6.5, 3.7, 3.1, and 3.1 folds with respect to C₃N₅, suggesting that S doping can significantly upgrade the property of C₃N₅ in the photocurrent response. Moreover, from the Electrochemical impedance spectroscopy (EIS) Nyquist curves of C₃N₅ and S-C₃N₅_0.1, we can see that the charge-transfer resistance of S-C₃N₅_0.1 is smaller than C₃N₅ (Fig. 4B), indicating that S doping lowers the charge-transfer resistance of C₃N₅. Upon visible light irradiation, the charge-transfer resistance of S-C₃N₅_0.1 becomes smaller and is also smaller than that of visible-light-irradiation C₃N₅. It can be concluded that S doping can efficiently upgrade the electrical conductivity of C₃N₅ by lowering the charge-transfer resistance, which well contributes to the separation and transfer of the photogenerated carriers in the photocatalytic process. This result well supports the result from the transient diffuse reflectance spectra (Fig. 3).

The optical properties of the C₃N₅ before and after S doping were further investigated by the UV-vis NIR diffuse reflectance spectra. Fig. 4 C and S4 show that all the S-C₃N₅ samples exhibit a redshift in the absorption edge compared to pristine C₃N₅, indicating the enhanced visible-light harvesting ability after S doping. Moreover, even though two absorption states assigned to the $\pi-\pi^*$ and $n-\pi^*$ electronic

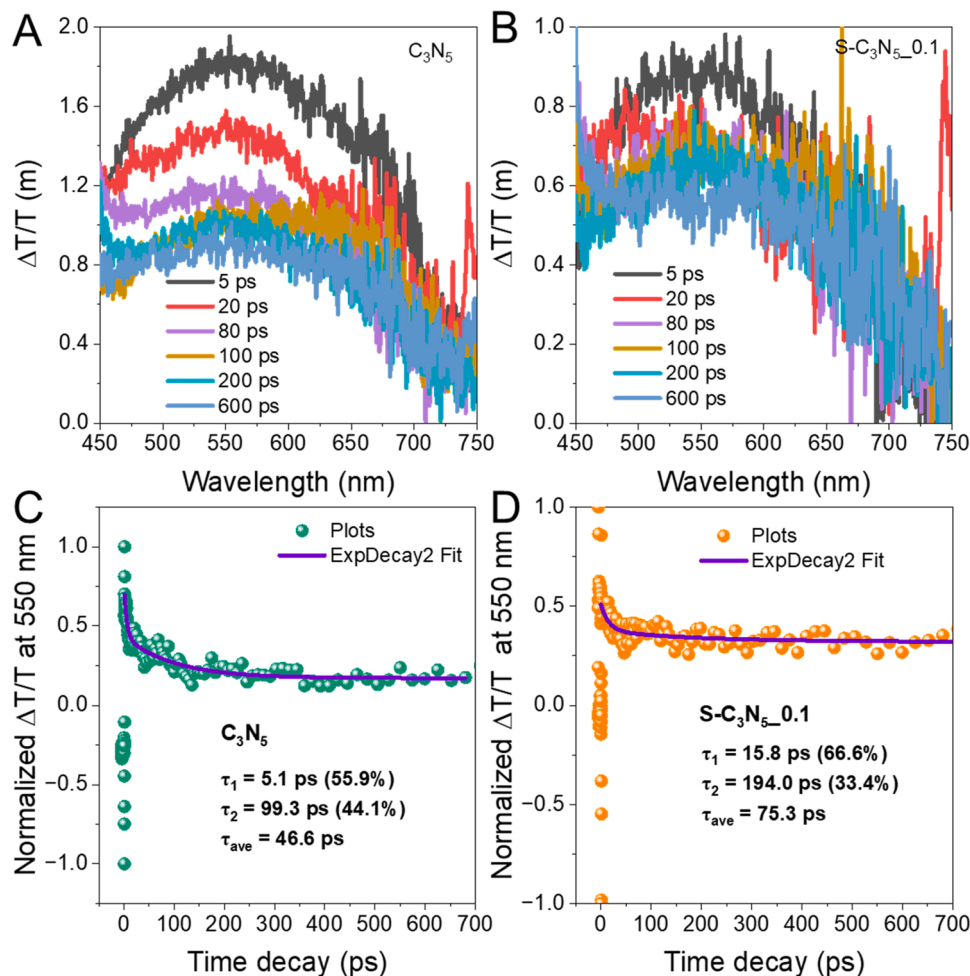


Fig. 3. (A-B) The transient diffuse reflectance spectra observed in the visible region by TDR spectra and (C-D) transient decay kinetics of C_3N_5 and $S-C_3N_5\text{-}0.1$.

transition with the absorption shoulders between 400 and 450 and 450–1000 nm can be observed in the spectra of C_3N_5 and $S-C_3N_5$ [43], but the shoulder between 400 and 450 nm for $S-C_3N_5$ shows a lower intensity, while that between 450 and 900 nm exhibits a higher intensity, suggesting that S doping lowers the structural order as well as achieves a distortion of the polymeric unit [44,45], which is consistent with the result from ESR characterization shown in Fig. 2 F. Furthermore, the bandgap energies and valence band (VB) potentials of C_3N_5 and $S-C_3N_5$ (taking the $S-C_3N_5\text{-}0.1$ as the model) are calculated and confirmed by the plots of $(ahv)^{1/2}$ versus the $h\nu$ (eV) (Fig. 4D) and XPS valence band spectra (Fig. 4E), respectively. Based on the empirical equation: $E_{\text{CB}} = E_{\text{VB}} - E_g$ [46], the conductive band (CB) potentials of C_3N_5 and $S-C_3N_5$ are obtained, thus giving the energy band structures of C_3N_5 before and after S doping (Fig. 4 F). It can be seen that S doping further decreases the bandgap and lowers the potentials of the CB and VB. Such an effect caused by S doping in C_3N_5 can be well supported by the calculated band structures of corresponding C_3N_5 and $S-C_3N_5$ (Figure S5). Such a result means an increase in the light-harvesting capability of $S-C_3N_5$ as well as the reinforcement in its oxidation ability.

3.2. Enhanced performance of $S-C_3N_5$ in photocatalytic air NO oxidation

We used the reaction of the photocatalytic air NO removal under 15 % humidity to investigate the enhanced photo-activity of S-doped C_3N_5 in comparison to the pristine one. From Figures S6A and 5 A, it can be seen when no catalysts exist in the reaction system, the NO removal in the air doesn't take place while using the C_3N_5 and $S-C_3N_5$ as catalysts, the NO can be efficiently removed from the air, especially that using

C_3N_5 shows an upgraded removal. Moreover, when using 0.1 mmol dibenzyl disulfide as the sulfur source, the obtained $S-C_3N_5\text{-}0.1$ exhibits the best performance for air NO removal, the NO removal efficiency increases 4.9 folds compared to pristine C_3N_5 . To deeply understand the catalytic effect of $S-C_3N_5$ for NO removal, we further investigated the dynamics of the photocatalytic NO removal using the pseudo-first-order kinetic fitting formula, the detailed parameters were summarized in Table S2. From Figure S6B, the photocatalytic NO removal rates using the S-doped C_3N_5 catalysts are higher than that using pristine C_3N_5 , especially, since the optimal $S-C_3N_5\text{-}0.1$ made the NO removal achieve the highest rate of 0.0301 min^{-1} , which is the 5.1 folds that using pristine C_3N_5 (0.0059 min^{-1}). Such results give strong evidence from the NO removal capability and dynamics two aspects to demonstrate the superiority of S-doped C_3N_5 over pristine C_3N_5 in visible-light photocatalysis.

The ten runs for reusing $S-C_3N_5\text{-}0.1$ in photocatalytic air NO removal were performed to prove the reusability and stability of S-doped C_3N_5 . As seen in Fig. 5 C, the NO removal efficiency after stabilization only shows a slight decline from 73.1 % to 67.1 %. Moreover, the toxic NO_2 product always remains at around 10 % yield during the ten runs, which suggests the outstanding NO deep-oxidation capability of S-doped C_3N_5 . In addition, given the current 10 min of reaction, we further extended the reaction time to 30 min for the verification of the durability of $S-C_3N_5\text{-}0.1$ (Figure S7). It can be seen that the NO removal only declines from 78.0 % at 1 min to 65.9 % at 30 min, and which tends to a stabilization state from the 10 min, demonstrating the durability of $S-C_3N_5$.

Moreover, in view of the structure stability of sulfur-doped C_3N_5 , on one hand, we comparatively analyzed the XRD patterns of fresh and

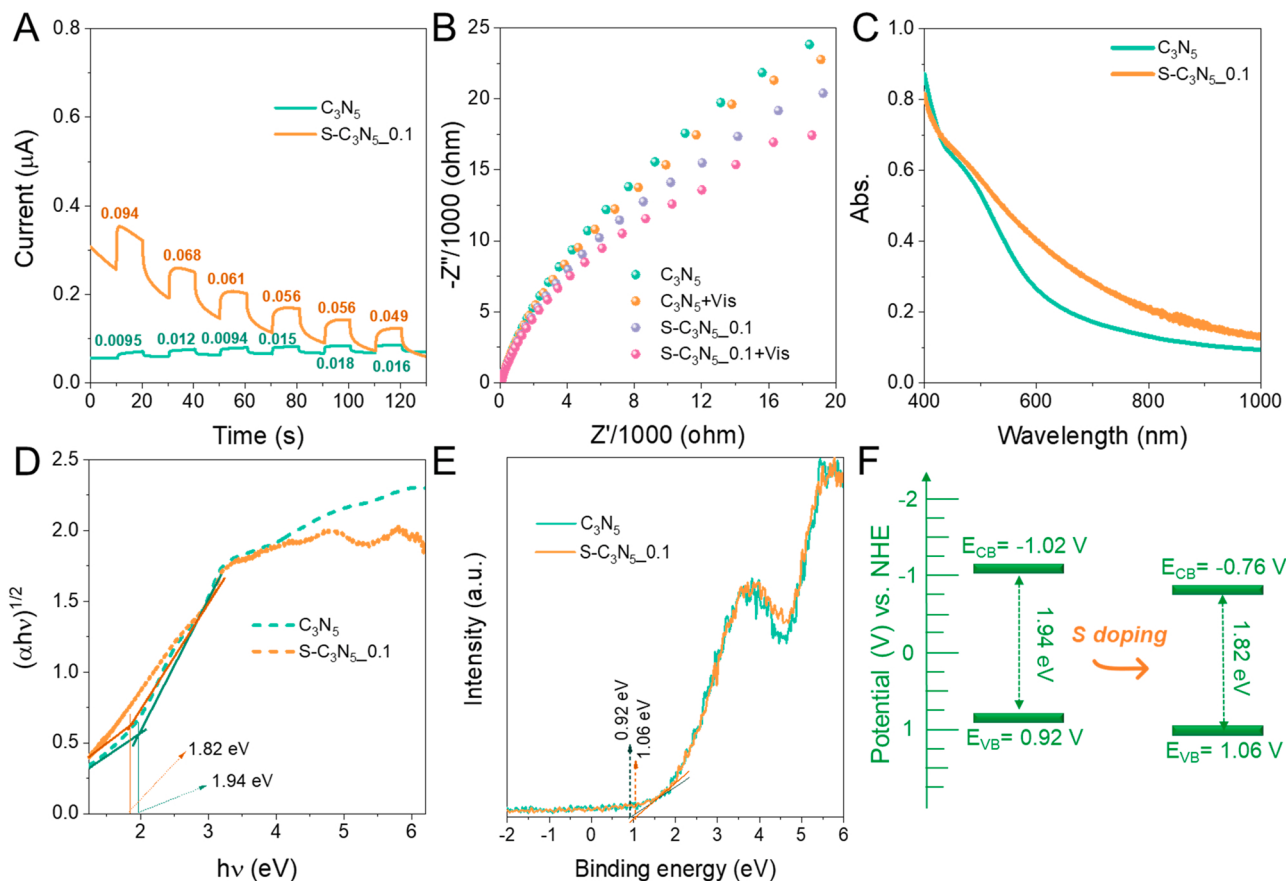


Fig. 4. (A) Transient photocurrent responses, (B) Electrochemical impedance spectroscopy (EIS) Nyquist plots whether using visible irradiation or not, (C) UV–vis NIR diffuse reflectance spectra, (D) the plots of $(\alpha(h\nu))^{1/2}$ versus the $h\nu$ (eV), (E) XPS valence band spectra, and (F) the electronic band structures of C_3N_5 and $\text{S-C}_3\text{N}_5\text{-}0.1$.

spent $\text{S-C}_3\text{N}_5\text{-}0.1$ samples, demonstrating the stable phase composition (Figure S8). On other hand, the *ab initio* molecular dynamics (AIMD) simulations were also used to investigate the stability of molecular structure of $\text{S-C}_3\text{N}_5$. Figure S9 presents the fluctuations of the Hartree-Fock energy calculated by AIMD. The energy changes within 10 ps remain a stable fluctuation state under 300 K, 400 K, and 500 K, which demonstrates the good stability of molecular structure of sulfur-doped C_3N_5 .

Furthermore, we investigated the performance data of photocatalytic NO removal over the C_3N_4 - and C_3N_5 -based catalysts from past ten years. As presented in Fig. 5D, it can be found that $\text{S-C}_3\text{N}_5$ exhibits stronger photocatalytic performance for NO removal than nearly all the C_3N_4 -based photocatalysts except for BP/ C_3N_4 -MOF, and is also more active than reported Ni- C_3N_5 and $\text{TiO}_2\text{-C}_3\text{N}_5$ as well as almost equal to few-layer C_3N_5 . Such results well demonstrate the superiority of S-doped C_3N_5 in the photocatalytic NO removal as well as the necessity to develop better C_3N_5 -based photocatalysts.

3.3. Analysis of the reason for enhanced photo-activity of $\text{S-C}_3\text{N}_5$ using DFT calculations

Apart from the characterization and performance evaluation, we further performed a series of density functional theory (DFT) calculations to investigate the origin of S-doped C_3N_5 showing an upgraded photo-activity. Firstly, we investigated the interaction between NO and C_3N_5 with(out) S doping based on the adsorption and charge density difference. Fig. 6 A shows the top-view images of the optimized charge density difference of the NO adsorbed on $\text{S-C}_3\text{N}_5$ and C_3N_5 . S doping makes the clear charge redistribution occur around the NO molecule.

The adsorption energy (E_{ads}), charge transfer ($|\Delta q|$), and bond length of N-O ($\text{l}_{\text{N-O}}$) after the NO molecule adsorbed on $\text{S-C}_3\text{N}_5$ are determined to be -1.79 eV, 0.56 e, and 1.92 Å, respectively, which are much bigger than those ($E_{\text{ads}}=-1.27$ eV, $|\Delta q|=0.32$ e, and $\text{l}_{\text{N-O}}=1.89$ Å) over pristine C_3N_5 . In brief, S doping endows C_3N_5 with stronger adsorption towards the NO molecule, more charge transfer with NO, and longer N-O bond length, which helps the next activation of NO for photocatalytic removal.

Furthermore, the free energy (ΔG) change trends of the NO molecule oxidation over $\text{S-C}_3\text{N}_5$ and C_3N_5 in the presence of O_2 were determined. As can be seen in Fig. 6B, the potential determining step locates at the third step, i.e., ${}^*\text{O}_2\text{-NO}$ species changes to ${}^*\text{O-NO}_2$ by overcoming a certain energy barrier. The energy barrier (1.71 eV) achieving the transformation from ${}^*\text{O}_2\text{-NO}$ species to ${}^*\text{O-NO}_2$ over pristine C_3N_5 is higher than that (1.46 eV) over $\text{S-C}_3\text{N}_5$, suggesting that NO photo-oxidation is easier to occur over $\text{S-C}_3\text{N}_5$ than pristine C_3N_5 . Besides, the free energies oxidizing NO molecules to NO_3^- species on $\text{S-C}_3\text{N}_5$ are lower than those using C_3N_5 , which means that products of NO conversion may include NO_2 , NO_3^- , and NO_3 , and $\text{S-C}_3\text{N}_5$ may achieve a better result.

Moreover, the projected density of states of C_3N_5 and $\text{S-C}_3\text{N}_5$ after adsorbing the NO molecule was further calculated. From Fig. S8, the $\text{S-C}_3\text{N}_5$ shows a much lower bandgap (0.77 eV) than C_3N_5 (1.84 eV) at this time. Besides, in comparison to that before adsorbing NO, the bandgap of $\text{S-C}_3\text{N}_5$ shows a 0.682 -eV decrease while a 0.46 -eV decline in the bandgap for C_3N_5 , which indicates the S atom in $\text{S-C}_3\text{N}_5$ has a strong interaction with the O atom in NO, further confirming the better adsorption capability of $\text{S-C}_3\text{N}_5$ towards NO.

To emphasize the superiority of the adsorption and activation of NO

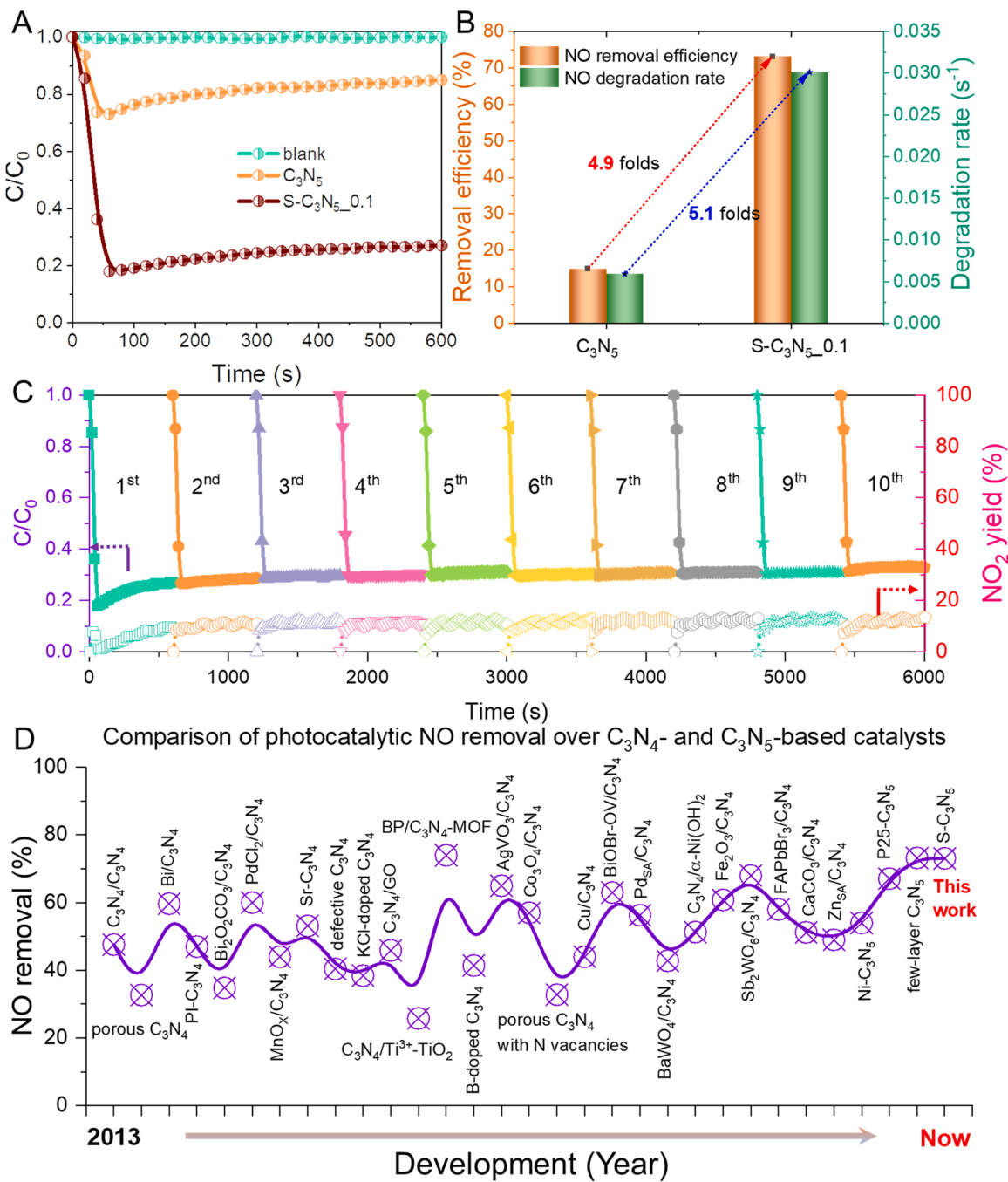


Fig. 5. (A) Photocatalytic air NO removal over C_3N_5 and $\text{S}-\text{C}_3\text{N}_5_{-0.1}$, (B) the comparison of NO removal efficiencies and rates, (C) the recycling NO removal experiments by reusing $\text{S}-\text{C}_3\text{N}_5_{-0.1}$, and (D) the comparison of the performance of reported C_3N_4 - and C_3N_5 -based photocatalysts for NO removal from 2013 to now.

molecules on the surface of $\text{S}-\text{C}_3\text{N}_5$, we further quantitatively evaluate the strength of the N-O bond through the integrated crystal orbital Hamilton population (ICOHP) analysis. The shorter bond length and larger value of -ICOHP indicate that the N-O bond is harder to break over C_3N_5 , which implies the NO oxidation pathway is not favored. As Fig. 6C-D shows that $\text{S}-\text{C}_3\text{N}_5$ is more favorable to activate the NO molecule than C_3N_5 , supporting S doping can facilitate the photocatalytic NO oxidation.

3.4. Identify the intermediates of air NO formed during the adsorption and photocatalysis over $\text{S}-\text{C}_3\text{N}_5$ by *in-situ* DRIFTS

As known, it is necessary and critical to investigate the intermediates

for a gas/solid heterogeneous reaction because the target gas molecules are always adsorbed on the active sites of a solid catalyst firstly and then are activated and transformed into the specific products. As illustrated in Fig. 7A, we analyzed the dark adsorption of NO molecules on $\text{S}-\text{C}_3\text{N}_5_{-0.1}$. From the changing trend of the *in-situ* DRIFTS spectra, it can be found that the adsorption-equilibrium of NO molecules on $\text{S}-\text{C}_3\text{N}_5_{-0.1}$ achieves within two minutes, indicating that acquired data from 2 min to 20 min can reflect the stabilization adsorption state of NO molecules on $\text{S}-\text{C}_3\text{N}_5_{-0.1}$. After achieving an adsorption-equilibrium state, in addition to the clear characteristic adsorption peaks of gas NO located at 913 cm^{-1} , 1020 cm^{-1} , and 1340 cm^{-1} , we can also observe those belonging to NO^{\cdot} at 1156 cm^{-1} and 1183 cm^{-1} , NO_2 at 1209 cm^{-1} , and NO_2^{\cdot} at 884 cm^{-1} , 1092 cm^{-1} , 1273 cm^{-1} , 1294 cm^{-1} , and 1318 cm^{-1}

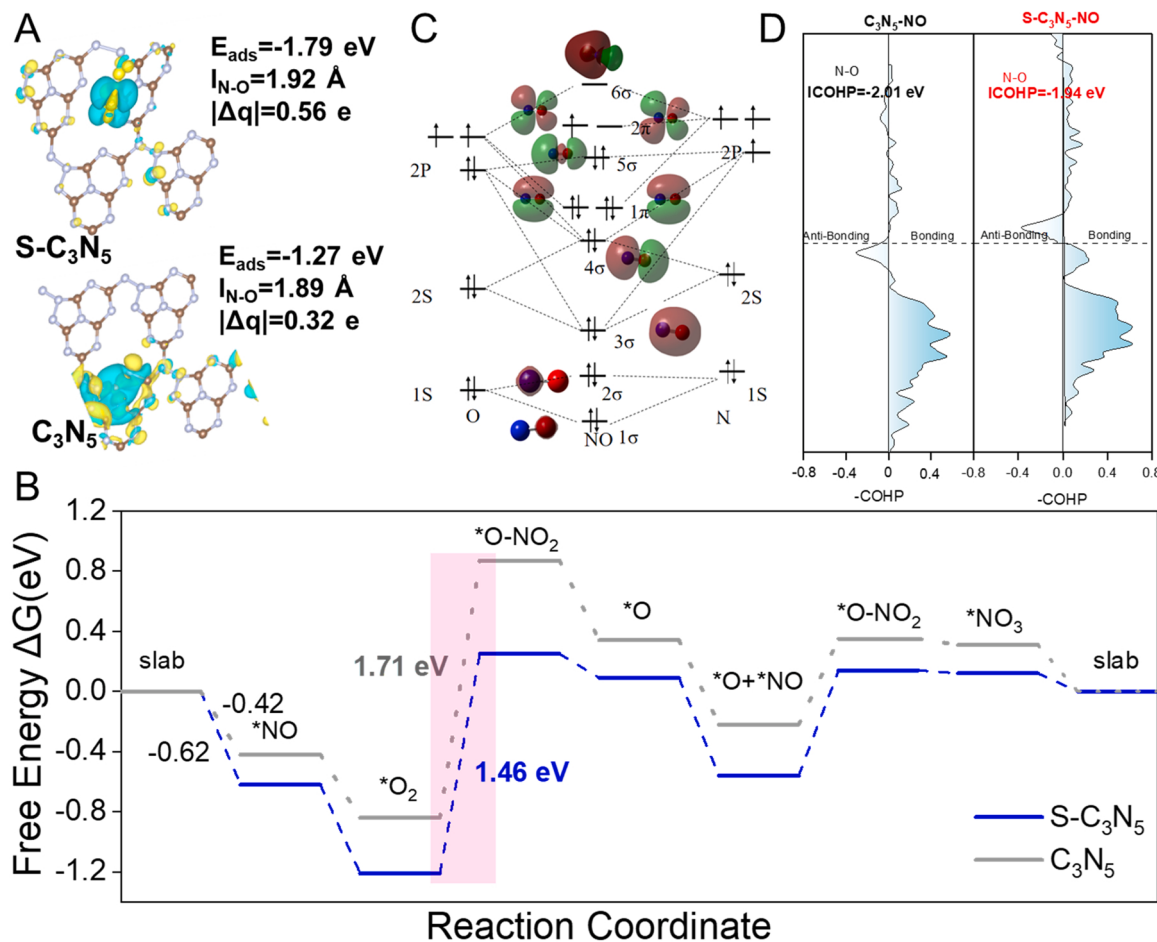


Fig. 6. (A) Optimized NO adsorption and charge density difference of C_3N_5 and $\text{S-C}_3\text{N}_5$, inset shows the corresponding E_{ads} , $l_{\text{N-O}}$, and $|\Delta q|$. (B) Density function theory (DFT) calculated the free energy of NO oxidation on C_3N_5 and $\text{S-C}_3\text{N}_5$. (C) The major interactions and energy levels of the molecular orbitals for the NO molecule. (D) The crystal orbital Hamilton population (COHP) binding analysis of NO on the C_3N_5 and $\text{S-C}_3\text{N}_5$ surface. The right and left sides of the figure show the antibonding and bonding interactions between the NO and C_3N_5 or $\text{S-C}_3\text{N}_5$, inset gives the integrated COHP (ICOHP) values.

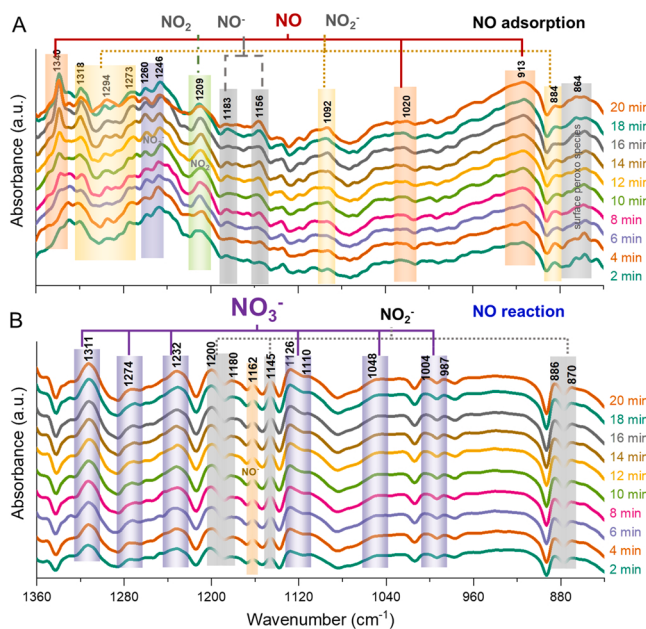


Fig. 7. *In-situ* DRIFTS spectra of $\text{S-C}_3\text{N}_5\text{.}0.1$ for NO adsorption in dark and photocatalytic oxidation under visible light irradiation.

[23,47–52]. The above-mentioned results suggest that S-doped C_3N_5 ($\text{S-C}_3\text{N}_5\text{.}0.1$) can effectively adsorb NO for the next activation and photocatalytic removal, while the observed NO_2 species may ascribe the oxidation by the surface per-oxo species as seen at 864 cm^{-1} .

Importantly, when the light source was turned on, the peaks belonging to NO and NO_2 disappear rapidly and thoroughly. Even though those peaks belonging to the NO^- and NO_2^- still existed, the number of corresponding peaks decreased clearly, especially for the former. In contrast, the peaks belonging to the NO_3^- swiftly appear at the wavenumber of 987 cm^{-1} , 1004 cm^{-1} , 1048 cm^{-1} , 1110 cm^{-1} , 1126 cm^{-1} , 1232 cm^{-1} , 1274 cm^{-1} , and 1311 cm^{-1} [53–55]. From such results, it can conclude that S-doped C_3N_5 ($\text{S-C}_3\text{N}_5\text{.}0.1$) can effectively change the toxic NO into the non-toxic NO_3^- under visible light irradiation, which is consistent with the results about the low NO_2 yield shown in Fig. 5 C. Together with the results of the dark adsorption, we summarized the process of NO adsorption and photocatalytic transform on $\text{S-C}_3\text{N}_5$. As presented in Fig. S9, when the NO and O_2 were adsorbed on $\text{S-C}_3\text{N}_5$, in the dark, part of the NO molecules may react with the surface O_2 and OH^- species to form NO_2 , NO_2^- , and NO^- ; Upon the irradiation of visible light, the NO molecules will be transformed into NO_3^- by the direct and indirect approaches.

3.5. The dominate active species identification and the mechanism establishment in the photocatalytic air NO removal over $\text{S-C}_3\text{N}_5$

To confirm the dominant active species responsible for the NO

removal in the system of visible-light driving S-C₃N₅ is the pre-condition for building the mechanism of photocatalytic NO conversion over S-C₃N₅. From Fig. 8 A, we find that potassium dichromate (K₂Cr₂O₇) plays an extreme inhibition on the NO removal in the system of visible-light driving S-C₃N₅, the NO removal efficiency at 10 min declines from 73.1 % to 15.1 %. Potassium iodide (KI) is the second one, making the NO removal efficiency decreased to 22.3 %. Relatively, the benzoquinone (BQ) and tert-butyl alcohol (TBA) nearly don't play a role in the NO removal, especially for the latter. Moreover, the electron spin resonance (ESR) spectra were further used to identify the reactive species in the presence of the reaction system. From Fig. 8B, the ESR signal of the 2,2,6,6-Tetramethylpiperidine 1-oxyl (TEMPO) free radical exhibits an obvious decline along with the irradiation of visible light, this is because it is reduced by coupling with the photogenerated holes (h^+) resulting from the S-C₃N₅ excited by the visible light. From Fig. 8 C, the obvious ESR signal of the 5,5-dimethyl-1-pyrroline N-oxide-superoxide radical (DMPO-O₂[·]) adduct is observed in the visible-light-driven S-C₃N₅ system while not any relative signals are observed during the dark reaction. In addition, we only observe the faint ESR signal of the 5,5-dimethyl-1-pyrroline N-oxide-Hydroxyl radical (DMPO-OH) adduct when the visible light irradiating S-C₃N₅ (Fig. 8D).

It can be concluded from the above results shown in Fig. 8A-D that the photogenerated electrons (e^-), holes (h^+), and superoxide radical ($\cdot O_2^-$) are responsible for the efficient NO removal in the system of visible-light driving S-C₃N₅, while the $\cdot OH$ is not the dominant active species, which can be attributed to the higher CB potential than that for O₂ to $\cdot O_2^-$ and lower VB potential than that for H₂O/OH[·] to $\cdot OH$. Combined with the results of the *in-situ* DRIFTS tests, the mechanism of photocatalytic air NO removal over S-C₃N₅ is thus proposed. As

illustrated in Fig. 8E, after being excited by the visible light, the photogenerated e^- and h^+ in the conductive band (CB) and valence band (VB) of S-C₃N₅ transfer rapidly to the surface of S-C₃N₅, and then react with the surface adsorbed NO and O₂ molecules. Through a series of redox reactions, the NO molecules are transformed to NO₃[·] under the attack of e^- , h^+ , and $\cdot O_2^-$ reactive species, completing the deep oxidation and toxic decline of toxic NO.

4. Conclusions

To conclude, sulfur doping strategy was adopted to enhance the performance of C₃N₅ for air NO photocatalytic removal. Compared to that using C₃N₅, S-C₃N₅ exhibits a 4.9-fold increase in the NO removal efficiency, and it can effectively make NO being deeply oxidized to NO₃[·]. Reasons behind such excellent photocatalytic activity are demonstrated as the reinforced photogenerated carriers' dynamics and h^+ oxidation capability, enhanced structural defects and improved NO and O₂ adsorption and activation. Ten runs in reuse in NO removal verify the stability of S-C₃N₅. A possible mechanism of photocatalytic air NO removal over S-C₃N₅ is proposed. This work contributes to the development of high-performance polymer carbon nitride-based photocatalysts for air NO_x abatement.

CRediT authorship contribution statement

Junlei Zhang: Conceptualization, Methodology, Data curation, Formal analysis, Writing – original draft, Funding acquisition. **Zhi Li:** Data curation, Formal analysis. **Bin Liu:** Data curation, Formal analysis. **Mengshan Chen:** Methodology, Formal analysis. **Yingtang Zhou:**

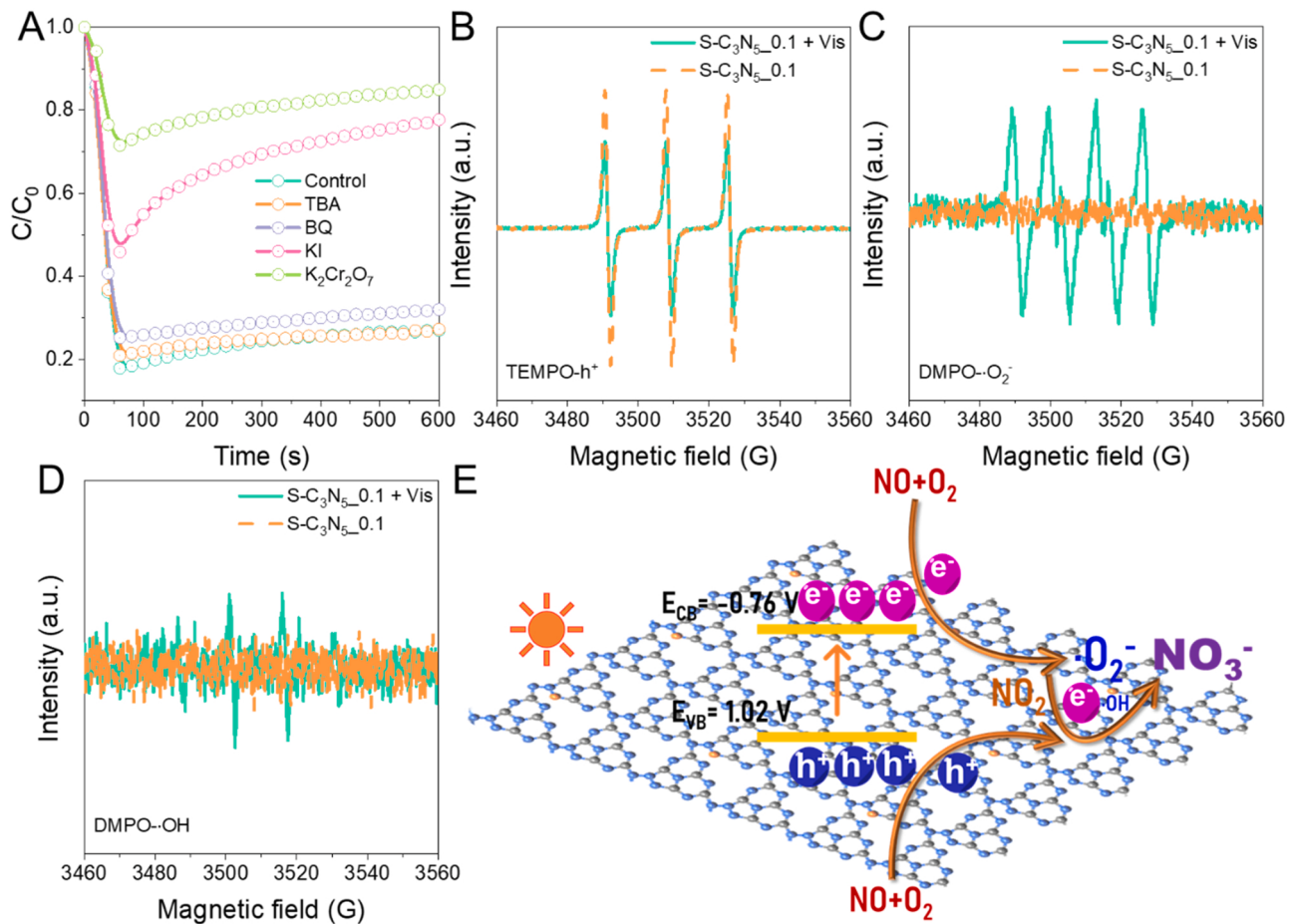


Fig. 8. (A) Effect on the NO removal over S-C₃N₅_0.1 under visible light when using different scavengers and (B-D) ESR spectra of TEMPO-h⁺, DMPO-O₂[·], and DMPO-OH adducts formed in the aqueous photocatalytic system. (E) The proposed possible reaction mechanism of NO removal over S-C₃N₅.

Methodology, Formal analysis, Funding acquisition. **Mingshan Zhu:** Conceptualization, Supervision, Writing – review & editing, Funding acquisition.

Declaration of Competing Interest

The authors declare that they have no known competing financial interests or personal relationships that could have appeared to influence the work reported in this paper.

Data Availability

Data will be made available on request.

Acknowledgments

This work was supported by the Guangdong Basic and Applied Basic Research Foundation (No. 2020A1515110482 and 2020B151502087), the Pearl River Talent Recruitment Program of Guangdong Province (2019QN01L148), the Natural Science Basic Research Program of Shaanxi (No. 2022JQ-334), the Fundamental Research Funds for the Central Universities (No. D5000210671), and the Zhejiang Province Key Research and Development Project (2023C01191).

Appendix A. Supporting information

Supplementary data associated with this article can be found in the online version at doi:10.1016/j.apcatb.2023.122522.

References

- [1] B. Mortazavi, F. Shojaei, M. Shahrokh, M. Azizi, T. Rabczuk, A.V. Shapeev, X. Zhuang, Nanoporous C₃N₄, C₃N₅ and C₃N₆ nanosheets; novel strong semiconductors with low thermal conductivities and appealing optical/electronic properties, *Carbon*, 167 (2020) 40–50.
- [2] G.P. Mane, S.N. Talapaneni, K.S. Lakhi, H. Ilbeygi, U. Ravon, K. Al-Bahily, T. Mori, D.-H. Park, A. Vinu, Highly ordered nitrogen-rich mesoporous carbon nitrides and their superior performance for sensing and photocatalytic hydrogen generation, *Angew. Chem. Int. Ed.* 56 (2017) 8481–8485.
- [3] P. Kumar, E. Vahidzadeh, W.K. Thakur, P. Kar, K.M. Alam, A. Goswami, N. Mandi, K. Cui, G.M. Bernard, V.K. Michaelis, K. Shankar, C₃N₅; a low bandgap semiconductor containing an Azo-linked carbon nitride framework for photocatalytic, photovoltaic and adsorbent applications, *J. Am. Chem. Soc.* 141 (2019) 5415–5436.
- [4] G. Zhang, M. Liu, T. Heil, S. Zafeiratos, A. Savateev, M. Antonietti, X. Wang, Electron deficient monomers that optimize nucleation and enhance the photocatalytic redox activity of carbon nitrides, *Angew. Chem. Int. Ed.* 58 (2019) 14950–14954.
- [5] H. Wang, M. Li, Q. Lu, Y. Cen, Y. Zhang, S. Yao, A. Mesoporous, Rod-like g-C₃N₅ synthesized by salt-guided strategy: as a superior photocatalyst for degradation of organic pollutant, *ACS Sustain. Chem. Eng.* 7 (2019) 625–631.
- [6] J.L. Zhang, B.H. Jing, Z.Y. Tang, Z.M. Ao, D.H. Xia, M.S. Zhu, S.B. Wang, Experimental and DFT insights into the visible-light driving metal-free C₃N₅ activated persulfate system for efficient water purification, *Appl. Catal. B-Environ.* 289 (2021), 120023.
- [7] Y. Lin, W. Su, X. Wang, X. Fu, X. Wang, LaOCl-coupled polymeric carbon nitride for overall water splitting through a one-photon excitation pathway, *Angew. Chem. Int. Ed.* 59 (2020) 20919–20923.
- [8] J. Xu, Q. Gao, Z. Wang, Y. Zhu, An all-organic 0D/2D supramolecular porphyrin/g-C₃N₄ heterojunction assembled via π-π interaction for efficient visible photocatalytic oxidation, *Appl. Catal. B-Environ.* (2021), 120059.
- [9] T. Liu, G. Yang, W. Wang, C. Wang, M. Wang, X. Sun, P. Xu, J. Zhang, Preparation of C₃N₅ nanosheets with enhanced performance in photocatalytic methylene blue (MB) degradation and H₂-evolution from water splitting, *Environ. Res.* 188 (2020), 109741-109741.
- [10] K. Li, W. Cai, Z. Zhang, H. Xie, Q. Zhong, H. Qu, Boron doped C₃N₅ for photocatalytic nitrogen fixation to ammonia: The key role of boron in nitrogen activation and mechanism, *Chem. Eng. J.* 435 (2022), 135017.
- [11] B. Debnath, S. Singh, S.M. Hossain, S. Krishnamurthy, V. Polshettiwar, S. Ogale, Visible light-driven highly selective CO₂ reduction to CH₄ using potassium-doped g-C₃N₅, *Langmuir* 38 (2022) 3139–3148.
- [12] C. Hu, Y.-H. Lin, M. Yoshida, S. Ashimura, Influence of phosphorus doping on triazole-based g-C₃N₅ nanosheets for enhanced photoelectrochemical and photocatalytic performance, *ACS Appl. Mater. Inter.* 13 (2021) 24907–24915.
- [13] H. Che, J. Wang, X. Gao, J. Chen, P. Wang, B. Liu, Y. Ao, Regulating directional transfer of electrons on polymeric g-C₃N₅ for highly efficient photocatalytic H₂O₂ production, *J. Colloid Interf. Sci.* 627 (2022) 739–748.
- [14] S. Vadivel, S. Hariganesh, B. Paul, G. Mamba, P. Puviarasu, Highly active novel CeTi₂O₆/g-C₃N₅ photocatalyst with extended spectral response towards removal of endocrine disruptor 2, 4-dichlorophenol in aqueous medium, *Colloid Surf. A-Physicochem. Eng. Asp.* 592 (2020), 124583.
- [15] S. Vadivel, S. Hariganesh, B. Paul, S. Rajendran, A. Habibi-Yangjeh, D. Maruthamani, M. Kumaravel, Synthesis of novel AgCl loaded g-C₃N₅ with ultrahigh activity as visible light photocatalyst for pollutants degradation, *Chem. Phys. Lett.* 738 (2020), 136862.
- [16] H. Yin, Y. Cao, T. Fan, M. Zhang, J. Yao, P. Li, S. Chen, X. Liu, In situ synthesis of Ag₃PO₄/C₃N₅ Z-scheme heterojunctions with enhanced visible-light-responsive photocatalytic performance for antibiotics removal, *Sci. Total Environ.* 754 (2021), 141926.
- [17] L. Wu, X. Yang, T. Chen, Y. Li, Q. Meng, L. Zhu, W. Zhu, R. He, T. Duan, Three-dimensional C₃N₅/RGO aerogels with enhanced visible-light response and electron-hole separation efficiency for photocatalytic uranium reduction, *Chem. Eng. J.* 427 (2022), 131773.
- [18] B. Wu, T. Sun, N. Liu, L. Lu, R. Zhang, W. Shi, P. Cheng, Modulation of Z-scheme heterojunction interface between ultrathin C₃N₅ nanosheets and metal-organic framework for boosting photocatalysis, *ACS Appl. Mater. Inter.* 14 (2022) 26742–26751.
- [19] Q. Meng, X. Yang, L. Wu, T. Chen, Y. Li, R. He, W. Zhu, L. Zhu, T. Duan, Metal-free 2D/2D C₃N₅/GO nanosheets with customized energy-level structure for radioactive nuclear wastewater treatment, *J. Hazard. Mater.* 422 (2022), 126912.
- [20] Z. Cai, Y. Huang, H. Ji, W. Liu, J. Fu, X. Sun, Type-II surface heterojunction of bismuth-rich Bi₄O₃Br₂ on nitrogen-rich g-C₃N₅ nanosheets for efficient photocatalytic degradation of antibiotics, *Sep. Purif. Technol.* 280 (2022), 119772.
- [21] S. Li, C. Wang, M. Cai, Y. Liu, K. Dong, J. Zhang, Designing oxygen vacancy mediated bismuth molybdate (Bi₂MoO₆)/N-rich carbon nitride (C₃N₅) S-scheme heterojunctions for boosted photocatalytic removal of tetracycline antibiotic and Cr(VI): Intermediate toxicity and mechanism insight, *J. Colloid Interf. Sci.* 624 (2022) 219–232.
- [22] S. Li, M. Cai, Y. Liu, J. Zhang, C. Wang, S. Zang, P. Zhang, X. Li, Y. Li, In-situ constructing C₃N₅ nanosheets/Bi₂WO₆ nanodots S-scheme heterojunction with enhanced structural defects for efficiently photocatalytic removal of tetracycline and Cr(VI), *Inorg. Chem. Front.* 9 (2022) 2479–2497.
- [23] J.L. Zhang, H. Tao, S. Wu, J. Yang, M. Zhu, Enhanced durability of nitric oxide removal on TiO₂ (P25) under visible light: Enabled by the direct Z-scheme mechanism and enhanced structure defects through coupling with C₃N₅, *Appl. Catal. B-Environ.* 296 (2021), 120372.
- [24] X. Bu, X. Liang, Y. Bu, Q. Quan, Y. Meng, Z. Lai, W. Wang, C. Liu, J. Lu, C.-M. Lawrence, Wu, J.C. Ho, NiMo@C₃N₅ heterostructures with multiple electronic transmission channels for highly efficient hydrogen evolution from alkaline electrolytes and seawater, *Chem. Eng. J.* 438 (2022), 135379.
- [25] B. Debnath, S.M. Hossain, A. Sadhu, S. Singh, V. Polshettiwar, S. Ogale, Construction of a 2D/2D g-C₃N₅/NiCr-LDH heterostructure to boost the green ammonia production rate under visible light illumination, *ACS Appl. Mater. Inter.* 14 (2022) 37076–37087.
- [26] W. Chu, S. Li, H. Zhou, M. Shi, J. Zhu, P. He, W. Liu, M. Wu, J. Wu, X. Yan, A novel bionic flower-like Z-scheme Bi₄O₅I₂/g-C₃N₅ heterojunction with I⁻/I₃⁻ active sites and π-conjugated structure for increasing photocatalytic oxidation of elemental mercury, *J. Environ. Chem. Eng.* 10 (2022), 108623.
- [27] H. Yang, W. Li, Y. Jiang, Q. Wei, L. Hou, Z. Wu, Q. He, Y. Wang, D. Tang, Diethylenetriamine-CdS hybrid materials (CdS-DETA) loaded nitrogen-rich carbon nitride (g-C₃N₅) for enhanced hydrogen production and photocatalytic degradation: enhancement based on band bending, *Sep. Purif. Technol.* 304 (2023), 122375.
- [28] F. Yi, J. Liu, G. Liang, X. Xiao, H. Wang, Insight into the enhanced degradation mechanism of g-C₃N₄/g-C₃N₅ heterostructures through photocatalytic molecular oxygen activation in Van der Waals junction and excitation, *J. Alloy. Compd.* 905 (2022), 164064.
- [29] S. Vadivel, M. Fujii, S. Rajendran, Facile synthesis of broom stick like FeOCl-g-C₃N₅ nanocomposite as novel Z-scheme photocatalysts for rapid degradation of pollutants, *Chemosphere* 307 (2022), 135716.
- [30] D. Liu, J. Yao, S. Chen, J. Zhang, R. Li, T. Peng, Construction of rGO-coupled C₃N₄/C₃N₅ 2D/2D Z-scheme heterojunction to accelerate charge separation for efficient visible light H₂ evolution, *Appl. Catal. B-Environ.* 318 (2022), 121822.
- [31] Q. Li, S. Song, Z. Mo, L. Zhang, Y. Qian, C. Ge, Hollow carbon nanospheres@graphitic C₃N₅ heterostructures for enhanced oxygen electroreduction, *Appl. Surf. Sci.* 579 (2022), 152006.
- [32] G. Li, G. Zeng, Z. Chen, J. Hong, X. Ji, Z. Lan, X. Tan, M. Li, X. Hu, C. Tang, In situ coupling carbon defective C₃N₅ nanosheet with Ag₂CO₃ for effective degradation of methylene blue and tetracycline hydrochloride, *Nanomaterials* 12 (2022) 2701.
- [33] L. Jiang, X. Yuan, Y. Pan, J. Liang, G. Zeng, Z. Wu, H. Wang, Doping of graphitic carbon nitride for photocatalysis: a review, *Appl. Catal. B-Environ.* 217 (2017) 388–406.
- [34] K. Wang, Q. Li, B. Liu, B. Cheng, W. Ho, J. Yu, Sulfur-doped g-C₃N₄ with enhanced photocatalytic CO₂-reduction performance, *Appl. Catal. B-Environ.* 176–177 (2015) 44–52.
- [35] G. Liu, P. Niu, C. Sun, S.C. Smith, Z. Chen, G.Q. Lu, H.-M. Cheng, Unique electronic structure induced high photoreactivity of sulfur-doped graphitic C₃N₄, *J. Am. Chem. Soc.* 132 (2010) 11642–11648.
- [36] Q. Liu, J. Shen, X. Yu, X. Yang, W. Liu, J. Yang, H. Tang, H. Xu, H. Li, Y. Li, J. Xu, Unveiling the origin of boosted photocatalytic hydrogen evolution in simultaneously (S, P, O)-Codoped and exfoliated ultrathin g-C₃N₄ nanosheets, *Appl. Catal. B-Environ.* 248 (2019) 84–94.

- [37] G.D. Fao, H.N. Catherine, C.-H. Huang, Y.-L. Lee, J.-C. Jiang, C. Hu, Unraveling the effects of P and S doping over g-C₃N₄ in strengthening Lewis basicity for CO₂/glycerol conversion: A theoretical and experimental study, *Carbon* 201 (2023) 129–140.
- [38] H. Zhang, Y. Chen, R. Lu, R. Li, A. Yu, Charge carrier kinetics of carbon nitride colloid: a femtosecond transient absorption spectroscopy study, *Phys. Chem. Chem. Phys.* 18 (2016) 14904–14910.
- [39] A. Kafizas, X. Wang, S.R. Pendlebury, P. Barnes, M. Ling, C. Sotelo-Vazquez, R. Quesada-Cabrera, C. Li, I.P. Parkin, J.R. Durrant, Where do photogenerated holes go in Anatase:Rutile TiO₂? A transient absorption spectroscopy study of charge transfer and lifetime, *J. Phys. Chem. A* 120 (2016) 715–723.
- [40] I.K. Sideri, Y. Jang, J. Garcés-Garcés, Á. Sastre-Santos, R. Canton-Vitoria, R. Kitaura, F. Fernández-Lázaro, F. D’Souza, N. Tagmatarchis, Unveiling the photoinduced electron-donating character of MoS₂ in covalently linked hybrids featuring peryleneimide, *Angew. Chem. Int. Ed.* 60 (2021) 9120–9126.
- [41] M.H. Elsayed, J. Jayakumar, M. Abdellah, T.H. Mansoure, K. Zheng, A.M. Elewa, C.-L. Chang, L.-Y. Ting, W.-C. Lin, H.-H. Yu, W.-H. Wang, C.-C. Chung, H.-H. Chou, Visible-light-driven hydrogen evolution using nitrogen-doped carbon quantum dot-implanted polymer dots as metal-free photocatalysts, *Appl. Catal. B-Environ.* 283 (2021), 119659.
- [42] M. Zhu, Z. Sun, M. Fujitsuka, T. Majima, Z-scheme photocatalytic water splitting on a 2D heterostructure of black phosphorus/bismuth vanadate using visible light, *Angew. Chem. Int. Ed.* 57 (2018) 2160–2164.
- [43] B. Zhai, H. Li, G. Gao, Y. Wang, P. Niu, S. Wang, L. Li, A crystalline carbon nitride based near-infrared active photocatalyst, *Adv. Funct. Mater.* 32 (2022), 2207375.
- [44] F. Ge, S. Huang, J. Yan, L. Jing, F. Chen, M. Xie, Y. Xu, H. Xu, H. Li, Sulfur promoted n-π* electron transitions in thiophene-doped g-C₃N₄ for enhanced photocatalytic activity, *Chin. J. Catal.* 42 (2021) 450–459.
- [45] C. Feng, L. Tang, Y. Deng, J. Wang, Y. Liu, X. Ouyang, H. Yang, J. Yu, J. Wang, A novel sulfur-assisted annealing method of g-C₃N₄ nanosheet compensates for the loss of light absorption with further promoted charge transfer for photocatalytic production of H₂ and H₂O₂, *Appl. Catal. B-Environ.* 281 (2021), 119539.
- [46] J.L. Zhang, Z. Ma, Ag₆Mo₁₀O₃₃/g-C₃N₄ 1D–2D hybridized heterojunction as an efficient visible-light-driven photocatalyst, *Mol. Catal.* 432 (2017) 285–291.
- [47] T. Cao, W. Huo, Z. Guo, C. Jing, Y. Chen, Y. Zhang, Z. Zhou, Constructing defective (BiO)₂CO₃ with different dominated facets for efficiently photocatalytic NO oxidation and in situ reaction pathway study, *Appl. Surf. Sci.* 498 (2019), 143848.
- [48] J. Zhang, Z. Li, J. He, H. Tao, M. Chen, Y. Zhou, M. Zhu, Reinforced photogenerated electrons in few-layer C₃N₅ for enhanced catalytic NO oxidation and CO₂ reduction, *ACS Catal.* 13 (2023) 785–795.
- [49] L. Han, J. Huang, J. Zhan, X. Zhang, S. Wang, H. Chen, Construction of highly dispersed Ni sites on N-rich carbon nitride for enhanced photocatalytic NO removal, *Adv. Sustain. Syst.* 7 (2023), 2200009.
- [50] Z. Guo, W. Huo, T. Cao, X. Liu, S. Ren, J. Yang, H. Ding, K. Chen, F. Dong, Y. Zhang, Heterojunction interface of zinc oxide and zinc sulfide promoting reactive molecules activation and carrier separation toward efficient photocatalysis, *J. Colloid Interf. Sci.* 588 (2021) 826–837.
- [51] Q. Ren, Y. He, H. Wang, Y. Sun, F. Dong, Photo-Switchable oxygen vacancy as the dynamic active site in the photocatalytic NO oxidation reaction, *ACS Catal.* 12 (2022) 14015–14025.
- [52] Z. Chen, H. Yin, R. Wang, Y. Peng, C. You, J. Li, Efficient electron transfer by plasmonic silver in SrTiO₃ for low-concentration photocatalytic NO oxidation, *Environ. Sci. Technol.* 56 (2022) 3604–3612.
- [53] Y. Yang, Y. Zeng, T. Jin, X. Zhang, H. Teng, S. Wang, H. Chen, Construction of oxygen vacancy on Bi₁₂O₇Cl₂ nanosheets by heat-treatment in H₂O vapor for photocatalytic NO oxidation, *J. Mater. Sci. Technol.* 123 (2022) 234–242.
- [54] W. Huo, W. Xu, Z. Guo, Y. Zhang, F. Dong, Motivated surface reaction thermodynamics on the bismuth oxyhalides with lattice strain for enhanced photocatalytic NO oxidation, *Appl. Catal. B-Environ.* 284 (2021), 119694.
- [55] W. Huo, T. Cao, W. Xu, Z. Guo, X. Liu, H.-C. Yao, Y. Zhang, F. Dong, Facile construction of Bi₂Mo₃O₁₂@Bi₂O₂CO₃ heterojunctions for enhanced photocatalytic efficiency toward NO removal and study of the conversion process, *Chin. J. Catal.* 41 (2020) 268–275.